Realizing Super-High Piezoelectricity and Excellent Fatigue Resistance in Domain-Engineered Bismuth Titanate Ferroelectrics

Xie, Shaoxiong
Institute for Advanced Study, Chengdu University

Xu, Qian
School of Architecture and Civil Engineering, Xihua University

Chen, Qiang
Department of Mechanical Engineering, Kyushu University

Zhu, Jianguo
College of Materials Science and Engineering, Sichuan University

他

出版情報：Advanced Functional Materials. 34 (18), pp.2312645-, 2024-01-20. Wiley
バージョン：
権利関係：

Realizing super-high piezoelectricity and excellent fatigue resistance in domain-engineered bismuth titanate ferroelectrics

Shaoxiong Xie[a,b,*,1], Qian Xu[c,1], Qiang Chen[b], Jianguo Zhu[d], Qingyuan Wang[a,*]

[a] Institute for Advanced Study, Chengdu University, Chengdu 610106, China

[b] Department of Mechanical Engineering, Kyushu University, Fukuoka 819-0395, Japan

[c] School of Architecture and Civil Engineering, Xihua University, Chengdu 610039, China

[d] College of Materials Science and Engineering, Sichuan University, Chengdu 610065, China

Abstract

Bismuth titanate (BIT) is widely known as one of the most prospective lead-free ferroelectric and piezoelectric materials in advanced high-temperature sensing applications. Despite significant advances in developing BIT ferroelectrics, it still faces major scientific and engineering challenges in realizing super-high performance to meet next-generation high-sensitivity and light-weight applications. Here, we conceived a novel ferroelectric domain-engineered BIT ceramic system that exhibits super-high piezoelectric performance (d_{33}~38.5 pC/N, d_{33}^{*}~46.7 pm/V at low electric field) and excellent fatigue resistance (stable up to 10^7 cycles). Our results reveal that the introduction of high-density layered (001)-type 180^o domain walls with flexible polarization rotation features and the formation of small-size multi-domain states with low energy barriers are mainly responsible for the excellent electrical performance. To our best knowledge, it is the first time to reveal such intriguing domain structures in BIT ceramics in detail, especially from the atomic-scale perspective by using Z-contrast imaging in combination with atomic-resolution polarization mapping. We believe that this breakthrough conduces to comprehensively understand structural features of ferroelectric domains in BIT ceramics, and also opens a window for future developments of

* Authors to whom the correspondence should be addressed: xsxdyx@126.com and wangqy@scu.edu.cn

[1] These authors contributed equally to this work

super-high performance in bismuth layer-structured ferroelectrics *via* domain engineering.

Keywords: Bismuth titanate; Electrical performance; Lattice distortion; Domain structures; Atomic-resolution polarization mapping

1. Introduction

Piezoelectric materials, which can directly interconvert mechanical energy and electrical energy, have been widely applied in various fields ranging from consumer electronics to high-end industries. With the rapid development of aerospace, geological exploration, and nuclear power generation, there has been a dramatic increase in the demand for high-temperature piezoelectric materials that can be operated at a temperature of 400 ^{o}C or greater[1]. Compared with commercial single-crystal piezoelectric materials, ferroelectric polycrystalline piezoelectric ceramics have aroused extensive research interests for the potential use in high-temperature sensing industries these years, due to the huge advantages in low costs and composition tunability[1a, 2]. Ferroelectric ceramics with the perovskite structure ABO_3, such as $Pb(Zr,Ti)O_3$, $BaTiO_3$, $K_{0.5}Na_{0.5}NbO_3$, and so forth, are by far the most used advanced electrical materials due to their excellent piezoelectric performance (d_{33}>400 pC/N)[3]. Nevertheless, low Curie temperature (T_c<350 ^{o}C) and lower ferroelectric phase boundary temperature prevent them from working in good order or even cause failure at high temperatures, making them non-competitive in high-temperature sensing techniques. It has been reported that bismuth layer-structured ferroelectrics (BLSFs), as an important branch of Aurivillius phase materials, possess high T_c (over 500 ^{o}C), good thermal stability, low aging rates, and lead-free features, which make them prospective to meet the requirements of functionality and reliability as well as environment-friendliness in high-temperature applications[4]. Among the BLSFs, bismuth titanate, $Bi_4Ti_3O_{12}$ (BIT), which is always regarded as the most promising candidate for advanced high-temperature sensing applications due to its higher Curie temperature (T_c~675 ^{o}C) and larger spontaneous polarization (P_s=50 μC/cm^2)[5]. However, the spatial rotation restriction of polarization vector **P** and low electrical resistivity as well as high leakage current density result in poor piezoelectric activity and low piezoelectric coefficient (d_{33}<8 pC/N) in pure BIT ferroelectric ceramics[6], significantly hindering their practical use in high-temperature electronic industries.

In recent decades, great efforts have been carried out to optimize the electrical performance of BIT ferroelectrics via different technical strategies, such as spark plasma sintering (SPS), template grain growth (TGG), molten salt (MS), chemical modification or ion doping, and the like[7]. Among these approaches, ion doping is widely taken as the most effective route to develop BIT ceramics with high performance and realize mass production since it enables easy tuning of sintering activity, microstructure, and electrical functionality at low costs. Extensive research has shown that a single substitution of BIT ceramics at B-site with high valence ions can greatly improve the piezoelectric performance[8]. For instance, by introducing the W^{6+} into the B-site of BIT ceramics, a large d_{33} of 20 pC/N can be achieved due to the simultaneous decrease in the conductivity and dielectric loss[8a]. However, for the single doping methods, the piezoelectric activity of BIT ceramics is still highly suppressed. Interestingly, the larger d_{33} of 26 pC/N has been reported in Nb^{5+}/Ta^{5+} dual-ion co-doped BIT ceramics[9]. Later, with the Mn^{4+}/Nb^{5+} dual-ion co-doping, the BIT ceramics attain a large resistivity and an enhanced piezoelectric performance (d_{33}~32.1 pC/N)[10]. In addition, the high piezoelectric activity and good dielectric properties are also realized in $Nb^{5+}/Ta^{5+}/Sb^{3+}$ multi-ion co-doped BIT ceramics[11]. Recent findings indicate that the A- and B-site substitutions in the perovskite layers of BIT ceramics are beneficial to optimizing the microstructures and tailoring resistivity behavior, resulting in improved piezoelectric behaviors with good thermal stability[12]. Despite the great advances in developing BIT ceramics by various ion-doping techniques, a further enhancement of electrical performance based on the existing optimization mechanism, such as tailoring oxygen vacancy concentration or altering microstructure features, to some extent, has reached a bottleneck. Therefore, developing novel strategies are required to realize the super-high performance of BIT ceramics to meet next-generation high-temperature applications that demand high-sensitivity and light-weight.

As it is widely known, the macro electrical performance of ferroelectric materials can be greatly manipulated by their underlying domain structures[13]. Accordingly, considerable trials have been performed to optimize the functional properties of piezoelectric ceramics by modifying the engineered domain structures[14], of which composition-driven structure design

strategy is the most popular. For instance, a high piezoelectric performance (d_{33}~755 pC/N) and an extremely large inverse piezoelectric coefficient (d_{33}^*~2027 pm/V) can be achieved in BT-based ceramics by manipulating underlying domain configuration utilizing chemical modification[14a]. In addition, it has been found that the formation of hierarchical nanodomain architecture in KNN-based ceramics by ion doping is responsible for the enhanced piezoelectric performance[14b]. At the same time, the ferroelectric domains could further transform into a slush polar state with multiphase coexistence by introducing $AgSbO_3$, which significantly decreases the energy barrier and polarization anisotropy, thus yielding an ultrahigh d_{33}~650 pC/N[14c]. For BIT ceramics, recent work has indicated that the excellent piezoelectric performance (d_{33}~30.5 pC/N) and high T_c~657 ^oC can be achieved by introducing Zn^{2+}/Nb^{5+} dual-ion to tailor ferroelectric domains[15]. A further enhancement of d_{33}~31.1 pC/N has been revealed in W/Cr co-doped BIT-based ceramics[16], which is attributed to the reduction of ferroelectric domain size by chemical modification. One can well perceive that there exists a great potential for domain engineering in optimizing electrical performance and exploring fundamental physical phenomena in BIT ceramics by such a composition-driven structure design strategy. However, current research on domain-engineered BIT ferroelectric ceramics is very limited, and the structural analysis of ferroelectric domains is also ambiguous. Therefore, the main conception in this work is to explore a novel domain engineering strategy to realize super-high performance in BIT ceramics, simultaneously understand the structural features of ferroelectric domains, and unravel their underlying mechanisms in optimizing performance.

Recent reports on W^{6+}/Nb^{5+} dual-ion co-doped BIT piezoelectric ceramics have shown improved piezoelectric properties (d_{33}~32 pC/N) and high electrical resistivity[17], which sheds a promising candidate in high-temperature electronic devices. In addition, it has been proved that Ce^{4+} ion-modified dual-ion co-doped BIT ceramic system exhibits a significant evolution of ferroelectric domain configuration with dopants, enabling further enhancing piezoelectric performance with good temperature stability[18]. Moreover, excellent piezoelectric performance has been successively reported in Ce, W, Nb multi-ion co-doped BIT-based ceramics via tailoring sintering temperatures and domain engineering[7e, 19]. They

attribute the enhanced performance to the significant evolutions of ferroelectric domains in ceramics by the introduction of dopants. Based on these considerations, we conceived a novel multi-ion co-doped BIT ceramic system with the chemical formula of $Bi_{3.96}Ce_{0.04}Ti_{3-0.02x}W_{0.01x}Nb_{0.01x}O_{12}$ (BCTWN) via composition-driven domain engineering strategy, where the domain structures can be manipulated by different dopant contents, while the electrical performance can be determined by the underlying ferroelectric domains. As expected, we achieved a super-high d_{33}~38.5 pC/N, nearly 5 times larger than pure BIT ceramics. Most importantly, an ultra-high d_{33}^*~46.7 pm/V (at low electric field) and an excellent fatigue behavior (only a 4% decrease in ferroelectric polarization up to 10^7 cycles) were also realized. To unravel the structural origin of enhanced performance, the ferroelectric domains were characterized by multi-scale microscopy techniques, and the atom displacement inside domains and atomic-resolution polarization mapping were performed by Z-contrast imaging, along with the ferroelectric domain switching behaviors and polarization dynamic features elaborated. It reveals that introducing high-density layered (001)-type 180^o domain walls (DWs) tends to tailor the domain structures in BIT ferroelectrics, significantly enhancing the electrical properties. This work sheds insight into performance optimization and practical use of BIT ceramics *via* domain engineering.

2. Results and Discussion

2.1. Crystal structure and sintering characteristics

The fresh BCTWN ceramics present plate-like grain morphology (Figure S1, Supporting information), which is the typical microstructure feature in BLSFs, since lower surface energy of (001) *plane* in layered crystal structure leads to a faster growth rate along *ab-plane* (grain length) than that along *c*-axis direction (grain thickness) during sintering process (Figure S1i, Supporting Information)[20]. Evidently, the dopants could effectively evolve the ions attachment or diffusion rates along the *ab-plane* and *c*-axis as indicated by the microstructures of BCTWN ceramics (Figure S1, S2, Supporting information), which thereby result in a significant variation tendency of first gradual increase and then rapid decrease in both grain length and thickness with the increase of doping content (Figure S3a, Supporting information). The microstructural evolutions are generally related to sintering kinetics of ceramic materials

affected by sintering temperature and concentration of oxygen vacancy. As it is widely known, a higher sintering temperature contributes to the increase of grain size of ceramics[21]. Besides, the samples with more vacancies have stronger grain boundary diffusion coefficients[22], which can accelerate the mass transport process with faster grain boundary migration and thus increase grain size. Therefore, for the ceramics with low doping contents ($x \leq 1.75$), the gradual increase in grain size is mainly attributed to the increase of sintering temperature, while for the rest of ceramics with high doping contents ($x \geq 2.00$), they have the same sintering temperatures, thus the decrease in grain size is mainly related to the decrease of grain boundary diffusion coefficients caused by the reduction of the concentration of oxygen vacancy due to the continuous addition of the high valence doping ions. In addition, the micro-pores were observed on the surface of the ceramics (Figure S2, Supporting information), which also are common features in BLSFs due to the lower packing density of the plate-like grains. The ceramic with x=1.75 presents the lowest density and relative density due to the largest plate-like grains among other compositions (Figure S3b, Supporting information), causing significant difficulties in having high packing density. However, the relative density of BCTWN ceramics remains more than 93%, higher than many reported BIT-based ceramics, suggesting that the BIT ceramics were well synthesized with better compactness and quality by the present dopant modification. This merit not only benefits the poling process of ceramics at high electric fields to enhance the electrical performance, but also improves the crack growth resistance at external stress to endow robust mechanical properties[21, 23].

Figure 1a shows the XRD patterns of BCTWN ceramics, and all samples possess a pure $Bi_4Ti_3O_{12}$-type Aurivillius phase, with no second phase detected in the diffraction peaks, reflecting no impurity particles generated in the sintering process, which could be further verified by the only existing plate-like grains in scanning electron microscopy (SEM) micrographs (Figure S1, S2, Supporting information). It is worth noting that the most intense diffraction peak of the samples is located at (117) reflection, which is in agreement with the fact that the strongest reflection of BLSFs is all of the types of (1 1 (2n+1)) (n represents the number of TiO_6 octahedron layer in the crystal structure, and it is 3 for BIT phase). To better

understand the perovskite phase structure of BCTWN ceramics, Figure 1b shows the high-resolution transmission electron microscopy (HRTEM) images of BCTWN ceramics taken along [110] zone-axis, revealing a nano-scale microstructure feature with the periodic lattice fringes as observed in the lower inset, together with the interplanar spacing $d_{(002)}$ of 1.639 nm confirmed by combination with the analysis of fast Fourier transform (FFT) pattern in the upper inset. The magnified HRTEM image shows atomic arrangement features of the layered lattice structure, including fluorite layers (Bi_2O_2 layers) and perovskite layers (TiO_6 octahedron layers), with no defects such as dislocations observed there, revealing good crystalline quality. Note that the real atom column positions are incapable of being determined by the HRTEM technique, since the image contrasts are mainly dependent on the sample thickness (t) and defocus (Δf), which has been elaborated in many previous work[24].

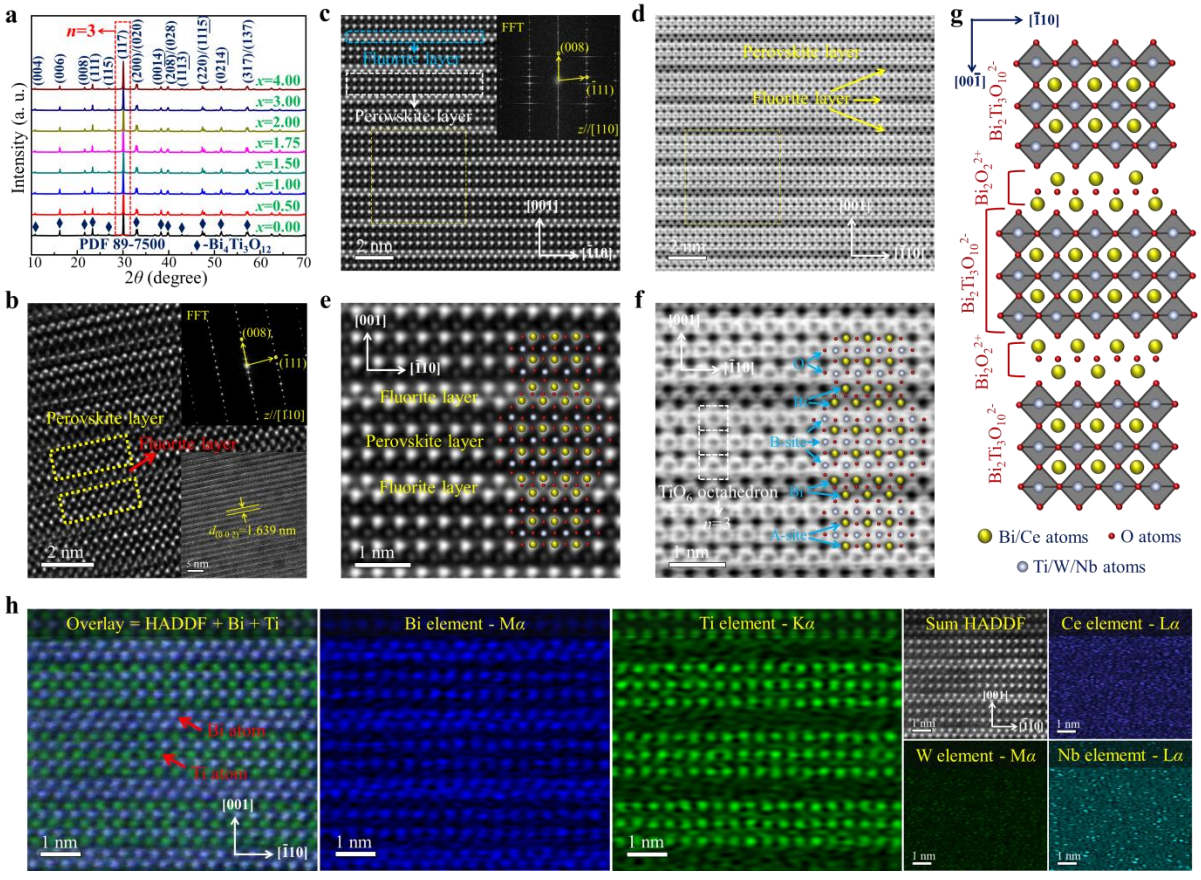

Figure 1. Structural characterization of BCTWN ceramics. a) XRD patterns of BCTWN ceramics with different doping contents. The blue rhomb represents the indexed $Bi_4Ti_3O_{12}$ phase. b) Atomic-scale HRTEM images of BCTWN-4.00 ceramics, taking along [110]

zone-axis. The lower inset in (b) shows a low magnification HRTEM image, while the upper inset shows the corresponding FFT pattern. c,d) HAADF- and ABF-STEM images of BCTWN-4.00 ceramics, observed along [110] zone-axis. The inset in (c) depicts the corresponding FFT pattern. e,f) Locally magnified HAADF- and ABF-STEM images of the yellow dotted rectangular boxes in (c) and (d), respectively. The atoms in fluorite layers and perovskite layers are overlaid on the images. g) The representative schematic of atomic crystal structure of BIT viewed from [110] zone-axis. h) Atomic-resolution STEM-EDS elemental mapping taking along [110] zone-axis.

For BIT ferroelectrics, the research on atom column distributions in the layered lattice structure is scarce. Therefore, to deeply understand the atomic-resolution structure features and reveal atom column distributions in BCTWN ceramics, the ceramic sample was performed by aberration-corrected scanning transmission electron microscopy (STEM) with high-angle angular dark-field (HAADF) and angular bright-field (ABF). Figure 1c,e shows the HAADF-STEM images observed along [110] zone-axis, directly revealing the layered lattice structure of the BIT phase at atomic-scale. In the HAADF-STEM mode, the image contrast is roughly proportional to the square of atomic number Z (Z is the average atomic number)[25]. Therefore, the bright and dim contrasts in the HAADF-STEM images represent Bi (Z=83) and Ti (Z=22) atom columns, respectively, while the doping atoms such as Ce (Z=58), W (Z=74), and Nb (Z=41) are hard to be detected in such atomic-scale due to very low content (less than 5%), although they are supposed to occupy the partial positions of the Bi atoms at A site and Ti atoms at B site in layered crystal structure of BCTWN ceramics. Figure 1d,f shows the corresponding ABF-STEM images, which allow us to directly visualize the light-element such as O atom columns in the presence of heavy atom columns[26]. The TiO_6 octahedron structures in perovskite layers could distinctly observed according to the ABF-STEM image contrast (Figure 1f). Evidently, each perovskite layer is composed of 3 TiO_6 octahedrons, further experimentally confirming that the n is 3 and the strongest reflection in BIT is (117) (Figure 1a). Moreover, the O atom columns are also directly visualized in fluorite layers, which are orderly distributed with nearby B atom columns, building up the Bi_2O_2 layers. To better confirm the atom column positions in ceramics, we

have performed an image simulation of crystal structure viewed along [110] zone-axis (Figure S4a, Supporting information). The representative schematic of crystal structure derived from the simulated structure model is well overlaid in the observed STEM images (Figure 1e,f,g), verifying the reliable assignment of image contrasts in STEM modes.

To shed light on the local elemental distributions in the lattice, we performed the atomic-resolution STEM energy-dispersive X-ray spectroscopy (EDS) elemental mapping of BCTWN ceramics taking along [110] zone-axis (Figure 1h). The elemental mapping of Bi-Mα and Ti-Kα X-ray intensities exhibits clear contrasts of Bi and Ti atom columns, with a periodic distribution in the layered lattice structure, of which the Bi atom columns occupy the fluorite layers and perovskite layers, while the Ti atom columns locate in the perovskite layers. The overlaid image comprising sum HADDF, Bi, and Ti elemental distribution maps directly reproduced the atomic arrangement feature in the layered lattice structure, which agrees well with the analysis of HAADF- and ABF-STEM images in Figure 1c,d,e,f. However, the elemental mapping of the doped Ce-Lα, W-Mα, and Nb-Lα X-ray intensities exhibits no typical contrasts of atom columns, which is attributed to only a small amount of the dopants in the sample and the effect of the inevitable noise in the mapping[27]. We also carried out the SEM-EDS elemental mapping of BCTWN ceramics, allowing us to identify individual elemental distribution at the micro-scale (Figure S5, Supporting information). One can see that all elements are detected and uniformly distributed in the elemental distribution maps, although the contents of the introduced elements are very low, confirming the dopants have successfully entered the BIT matrix due to similar ion radii and valence states among these ions (such as for A-site ions: r_{Bi}^{3+}=1.03 Å and r_{Ce}^{3+}=1.01 Å; for B-site ions: r_{W}^{6+}=0.60 Å, r_{Nb}^{5+}=0.64 Å, r_{Ti}^{4+} = 0.605 Å) and formed the ceramic solid solution.

To reveal the effect of dopants on crystal structural evolutions, we performed the Rietveld refinement of XRD patterns for BCTWN ceramics (Figure S6, Supporting information). The fitted diffraction patterns show a perfect match with the experimental data, with the lower value of the goodness of fit indicator (*Sig*) (Table S1, Supporting information), illustrating the reliable refinement results for the samples[28]. The lattice parameters are changed by adding dopants, leading to an increased orthorhombic distortion (*b/a*) of crystal structure in

BCTWN-1.75 ceramics (Table S1, Supporting information). In addition, as reported before, the structural distortion of BIT-based ferroelectrics mainly originates from TO_6 octahedron rotation on the *ab-plane* of crystal structure[7e, 12]. According to the atomic site occupation information of BCTWN ceramics (Table S2, Supporting information), the structural distortion was further analyzed on *ab-plane* (Figure S7, Supporting information). Notably, the TO_6 octahedron rotation angles of BCTWN ceramics with different compositions are distinct, and the BCTWN-1.75 ceramics exhibit the larger octahedron rotation on *ab-plane*, indicating a decreased symmetry and an enhanced lattice distortion of the layered crystal structure by the appropriate introduction of dopants. We also carried out Raman spectroscopy to elaborate the crystal structural evolutions of BCTWN ceramics (Figure S8, Supporting information). Evidently, the mode near 538 cm^{-1} in Raman spectra shifts to a lower frequency first and then to a higher frequency with the increase of doping content, implying that the lattice distortion is increased initially and subsequently decreased due to the significant change of the vibration modes of Ti-O band[29]. Moreover, the peak shapes seem to become more flattened with the appropriate addition of dopants. All these are the direct evidence of the crystal structural evolutions in BCTWN ceramics due to the addition of dopants.

2.2. Electrical performance

Figure 2a shows the temperature dependence of the dielectric constant (ε_r) of the BCTWN ceramics with different doping contents, measured at 1 MHz. There exists only a dielectric abnormality in the dielectric response curves of all samples, indicating the first-order phase transition from polar ferroelectric phase to nonpolar paraelectric phase in BLSFs. The dielectric peaks of the samples exhibit a sharp shape, and the corresponding Curie temperatures (T_c) remain unchanged at different applied frequencies (Figure S9a, Supporting information), demonstrating the features of normal ferroelectrics with the negligible diffuse phase transition behaviors and reflecting the frequency independent nature of BCTWN ceramics. The T_c presents a slight decrease with the increase of doping level, while it still keeps above 631 ^oC, strongly suggesting the good prospect of the ceramic system in high-temperature applications. We also deduced the dielectric temperature coefficient (Tk_ε) to reveal the thermal stability of dielectric properties of BCTWN ceramics (Figure S9b,c,

Supporting information). The Tk_ε is slightly increased with the increase of temperature, and as the temperature is up to 500 °C, whose value remains below 1.50×10^{-3}/ ℃, indicating that the BCTWN ceramics have a good dielectric thermal stability that enables a wide operation temperature in practical use.

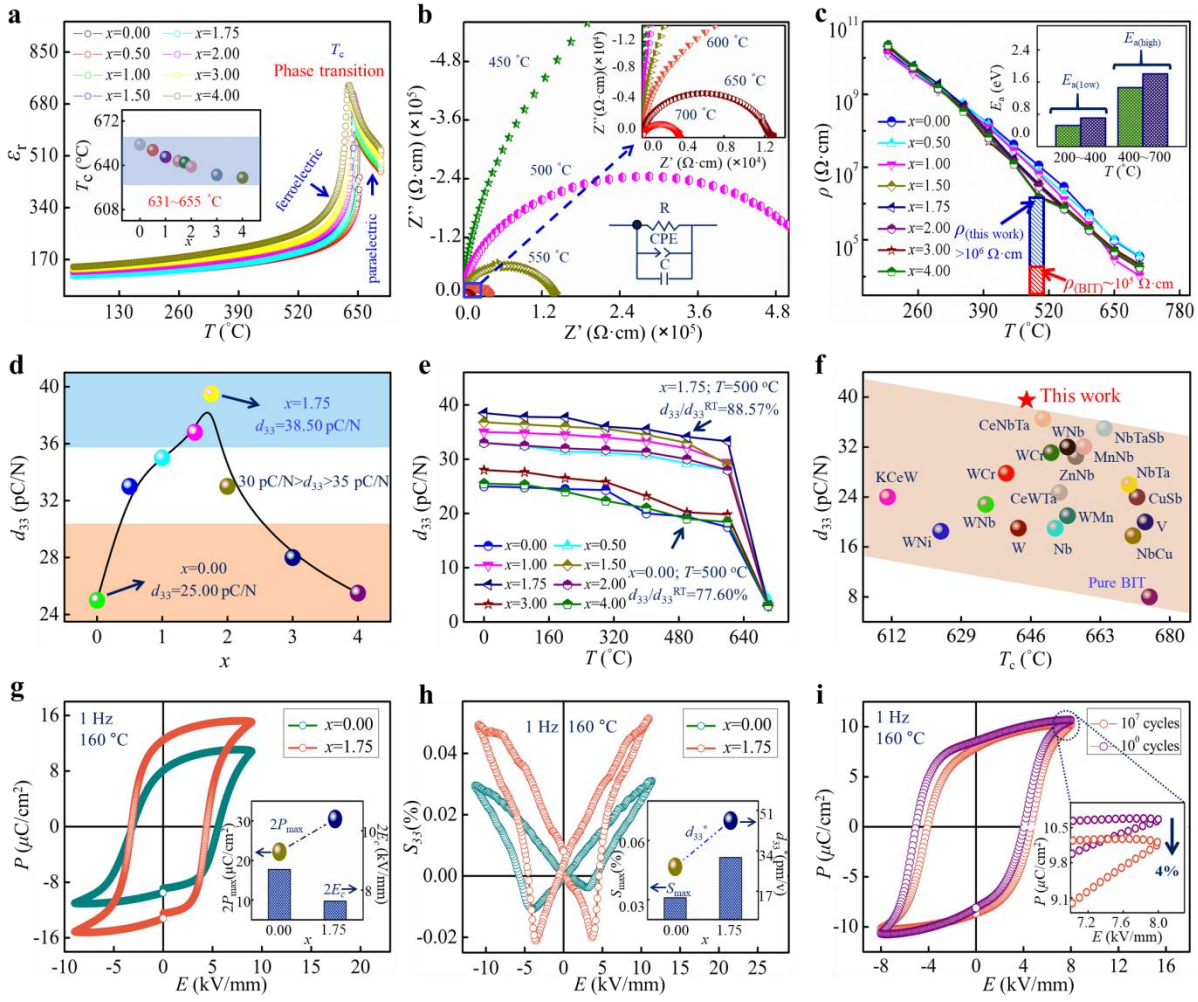

Figure 2. Electrical properties of BCTWN ceramics. a) Dielectric-temperature curves of BCTWN ceramics with different doping contents. The inset depicts T_c as a function of doping content. b) Nyquist plots of BCTWN-1.75 ceramics at different temperatures. Z' and Z'' are the real and imaginary part of impedance, respectively. The inset represents the corresponding fitting equivalent circuit. c) Temperature dependence of the ρ of BCTWN ceramics with different doping contents. The inset depicts the ranges of E_a for all BCTWN ceramics at low-temperature region (200-400 °C) and high-temperature region (400-700 °C), of which E_a is located in the range of 0.52-0.71 eV at low-temperature region, while it is around 1.46-1.87

eV at high-temperature region. d) The d_{33} of BCTWN ceramics as a function of doping content. e) The d_{33} of BCTWN ceramics at different annealing temperatures. f) A comprehensive comparison of d_{33} and T_c of BIT-based ceramics. g,h) Ferroelectric *P-E* hysteresis loops and *S-E* butterfly curves of BCTWN-0.00 and BCTWN-1.75 ceramics, respectively. The insets denote the corresponding ferroelectric parameters. i) Electric fatigue *P-E* hysteresis loops of BCTWN-1.75 ceramics. The inset is the locally enlarged curves in (i).

The electrical resistance is an important figure of merit that greatly affects the practical use of ferroelectric materials, especially at high temperatures. To reveal the resistance behaviors of BCTWN ceramics, the Nyquist plots of the samples were tested at different temperatures (Figure 2b; Figure S10, Supporting information). There is a single semicircle observed in the complex impedance plots of all samples, and the experimental data could be fitted by a simplified equivalent circuit of resistor (R) with only a shunted constant phase element (CPE), as shown in the inset of Figure 2b, indicating that the ceramics are electrically homogeneous and the resistance behaviors are mainly associated with a grain (bulk) response[30]. As the temperature increases, the diameter of the semicircle decreases, indicating a decrease in the electrical resistance at higher temperatures, which is related to the thermally activated charge carriers. To further explore the conductivity of BCTWN ceramics, we performed the DC resistivity (ρ) of the samples at different temperatures (Figure 2c). Clearly, the resistivity of the ceramics reduces with the increase in temperature, which is consistent with the results in Nyquist plots. Interestingly, the BCTWN ceramics present a higher electrical resistance than pure BIT ceramics. For instance, the resistivity of BCTWN ceramics at 500 ^{o}C exceeds 1×10^{6} Ω·cm, which is more than one order of magnitude higher than that of pure BIT ceramics. Such high resistivity enables to decrease the charge drift interfered by piezoelectric-induced charges, beneficial for enhancing the stability of piezoelectric ceramics working at high temperatures. Here, the improvement of resistivity in BCTWN ceramics is mainly attributed to the decreased oxygen vacancy concentration due to the introduction of the high valence doping ions, which has been extensively reported elsewhere[31]. In addition, to elaborate on the conduction mechanism, the activity energy (E_a) during the conduction process was extracted by fitting the relationship between temperature and logarithmic resistivity of

BCTWN ceramics according to the Arrhenius equation (Figure S11, Supporting information)[32]. It is worth noting that the conduction behaviors of BCTWN ceramics are characterized by two different temperature regions in the range of 200-700 ^{o}C (Figure 2c; Figure S11, Supporting information). The ceramics at low-temperature region (200-400 ^{o}C) present the activation energy of 0.52-0.71 eV, indicating that the extrinsic semiconductor charge carriers (p-type), such as the mobility of oxygen vacancies, dominate the conductivity mechanism. While the activation energy is around 1.46-1.86 eV at the high-temperature region (400-700 ^{o}C), whose value is close to half of the theoretical band gap energy (3.3 eV) of BIT ferroelectrics, strongly reflecting the intrinsic conduction of the ceramics dominated at high temperatures. Similar findings have been revealed in other BIT-based piezoelectric ceramic systems[18, 30, 32].

Figure 2d shows the piezoelectric properties of BCTWN ceramics at room temperature. One can see that the piezoelectric coefficient (d_{33}) is increased first and then decreased with the increase of doping content, suggesting that the dopants could significantly alter the piezoelectric properties. Importantly, a super-high d_{33} of 38.50 pC/N is achieved in BCTWN-1.75 ceramics, which is close to 5 times larger than pure BIT ceramics. To reveal the thermal stability of the piezoelectric properties, the d_{33} of BCTWN ceramics were also characterized at different annealing temperatures ranging from room temperature to 700 ^{o}C (Figure 2e). The d_{33} values of BCTWN ceramics present a slight variation with the increase in annealing temperature. Interestingly, the BCTWN-1.75 ceramics exhibits a larger d_{33} of more than 34 pC/N, i.e., retaining over 88% of its room temperature value as the temperature exceeds 500 ^{o}C, suggesting good thermal stability and beneficial to the high-temperature applications. Moreover, it is clear that the d_{33} of BCTWN ceramics in this work is superior compared with other reported BIT-based ceramics[6, 7d, 8-12, 15-18, 31, 33], together with a higher T_c (Figure 2f). We believe this will be a breakthrough in the performance optimization of BIT piezoelectric ceramics, and the BCTWC ceramics with such super-high piezoelectric performance shed great potential to meet next-generation high-sensitivity and light-weight requirements in high-temperature applications.

In addition to the excellent piezoelectric properties, the BCTWN-1.75 ceramics also exhibit

the best ferroelectric properties among other BCTWN compositions, which is strongly supported by the slimmer electric-field induced polarization (*P*-*E*) hysteresis loops and classical electric-field induced strain (*S*-*E*) butterfly curves (Figure 2g,h; Figure S12, Supporting information). Accordingly, the largest ferroelectric polarization ($2P_{max}$=30.46 μC/cm^2) and ferroelectric strain (S_{max}=0.0514%) are realized in BCTWN-1.75 ceramics, together with the lowest coercive field ($2E_c$=7.63 kV/mm). Here, the resulting ferroelectric polarization is smaller than that (P_s = 50 μC/cm^2) obtained in BIT single crystal, which is attributed to the fact that it is difficult for polycrystalline BCTWN ceramics to be completely poled under applied electric fields due to the existence of more domain walls, grain boundaries, and micro pores in the matrix. It is worth noting that a super-high inverse piezoelectric coefficient (d_{33}^*=46.7 pm/V) is attained in BCTWN-1.75 ceramics at a lower electric field (11 kV/mm), which is comparable to the current highest value (d_{33}^*=47 pm/V) realized at higher electric field (15 kV/mm) for BIT material systems[34], endowing the BCTWN ceramic with the promising applications in high-precision displacement or strain actuators. For ferroelectric materials, fatigue behavior is also very critical for their practical applications. The evolutions of *P*-*E* loops of BCTWN-1.75 ceramics under electric fatigue cycles are displayed in Figure 2i. Only a slight decrease (4%) in ferroelectric polarization is observed in *P*-*E* loops when the electric load reaches 10^7 cycles, indicating excellent fatigue stability of BIT ceramics by the present doping strategy.

As it is widely known, the piezoelectric response of ferroelectric materials originates from intrinsic (lattice structure) and extrinsic (domain structures) contributions[14b]. For the BCTWN ceramic system, the peak d_{33} occurs in the composition of x=1.75 (BCTWN-1.75) with a more distorted lattice structure (Figure S7, Supporting information), at this point corresponding to a larger ion displacement, together with a higher ferroelectric polarization as well as a larger ferroelectric strain (Figure 2g,h), leading to an enhanced piezoelectric property. Besides, considering the close relationship between domain structures and piezoelectric properties, we next employed chemical etching (CE), piezoresponse force microscopy (PFM), transmission electron microscopy (TEM), and STEM techniques to deeply understand the domain structures at multi-sized scales and further unravel the origin of

enhanced performance in BCTWN ceramics.

2.3. Domain structures and performance optimization mechanism

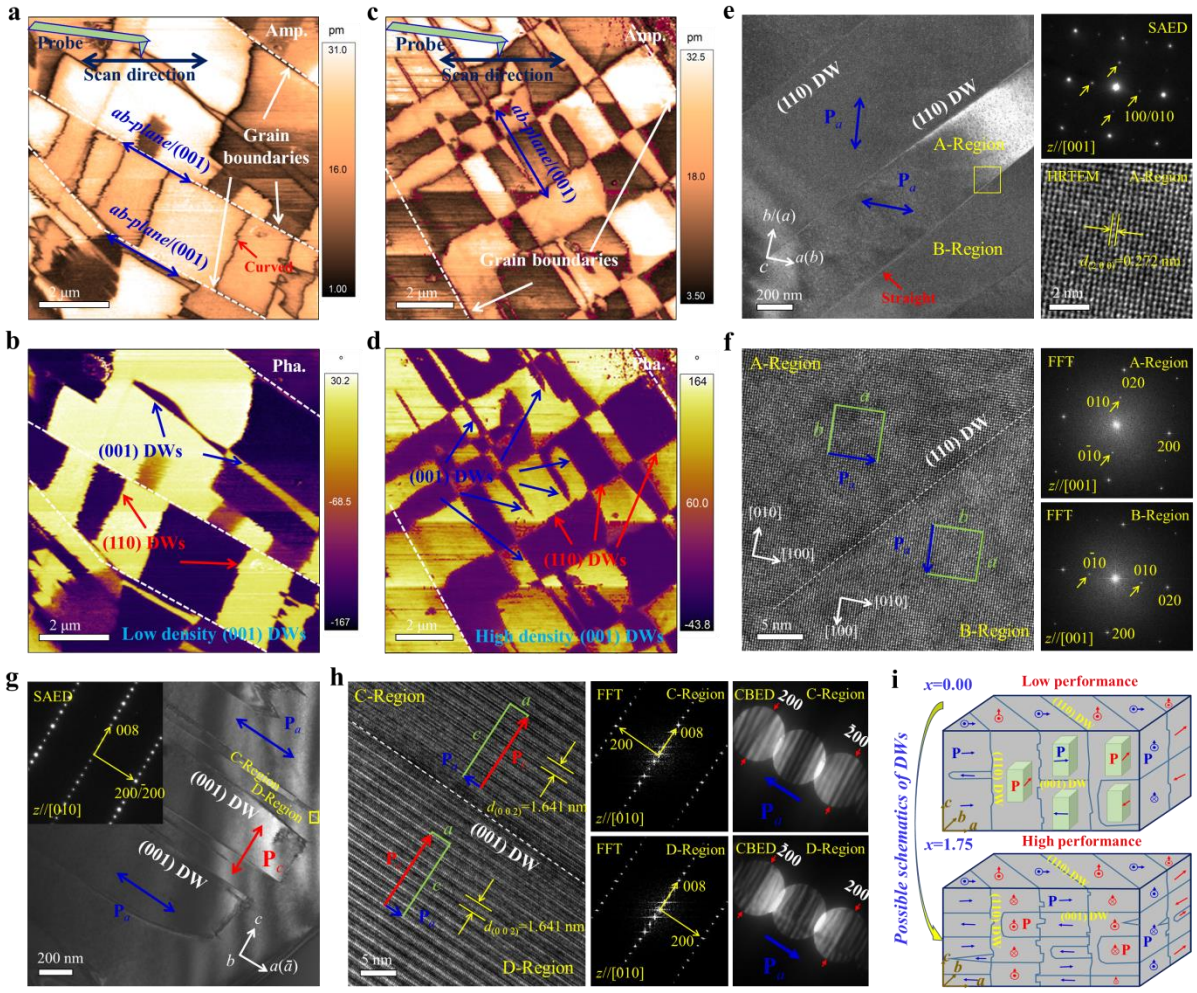

Figure 3. The characterization of domain structures in BCTWN ceramics. a,c) Vertical PFM amplitude and b,d) phase images of BCTWN-0.00 and BCTWN-1.75 ceramics, respectively. The inset means scan direction of PFM probe. e) DF-TEM image taking along [001] zone-axis. The images on the right represent corresponding SAED pattern and HRTEM image of A-Region in (e). f) HRTEM image of the yellow rectangular box including A- and B-Region in (e). The insets mean the schematics of crystal structure viewed along [001] direction. The images on the right depict FFT patterns of A- and B-Region, respectively. g) DF-TEM image taking along [010] zone-axis. The inset shows corresponding SAED pattern. h) HRTEM image of the yellow small rectangular box including C- and D-Region with a (001)-type domain wall in (g). The insets represent the schematics of crystal structure viewed

along [010] direction. The images on the right depict FFT patterns and CBED patterns of C- and D-Region in (g,h), respectively. i) The schematics of domain patterns in BCTWN ceramics with lower and higher performance, respectively. **P** respects the polarization vector in BIT ferroelectrics.

The microstructure features of BCTWN ceramics with chemical etching treatment are displayed in SEM micrographs (Figure S13, Supporting information). One can see that there exist different domain structure types in BCTWN ceramics, judged by the different SEM image contrasts and further verified by the different etching rates of the domain structures as indicated in atomic force microscopy (AFM) profile (Figure S14, Supporting information). Based on the unique anisotropic growth behavior of plate-like grain in BIT ferroelectrics, the *ab-plane* of grain could be confirmed as the crystallographic (001) *plane*, and the intersection line between the cross-section of grain and (001) *plane* is the grain boundary (Figure S2d,i, Supporting information). Accordingly, the domain types on the cross-sections of grains of BCTWN ceramics are roughly divided into two groups, where one is the domain wall (DW-I) marked by the red dotted line intersecting the grain boundary or *ab-plane*, while the other is the DW-II marked by the blue dotted line parallel to the *ab-plane* and located between DW-I (Figure S13a,c, Supporting information). Note that the DW-I could intersect the *ab-plane* at different angles that depend on the crystal plane in which DW-I is located. For instance, the angles of around 75^{o} and 90^{o} which DW-I intersects the *ab-plane* are indicated in the SEM image (Figure S13d, Supporting information), which represents these DWs located in the different crystal planes of BCTWN ceramics. Historically, the DW-I has been widely reported that it belongs to the (110)-type DW[24b, 35], while the DW-II is seldom reported so far in BIT ceramic systems. We here call it (001)-type DW since it lies on the crystallographic (001) plane. Compared with the BCTWN-0.00 ceramics with lower piezoelectric performance, the BCTWN-1.75 ceramics with super-high piezoelectricity exhibit exceedingly abundant (001)-type DWs with layered arrangement features along *c*-axis, which greatly split the previously larger domain stripes into numerous smaller domain segments with widths ranging from a few nanometers to hundreds of nanometers (Figure S13b,d, Supporting information). It follows that the appropriate dopants could introduce numbers of (001)-type DWs and destroy

the long-range ordered (110)-type domain structures in BIT ceramics, thus decreasing domain size and inducing multi-domain states with high DW density. Such novel domain structure evolutions are rarely revealed in other BIT ceramics.

To verify the above observations and further characterize the intriguing domain structures, we employed vertical PFM (VPFM) and lateral PFM (LPFM) to probe microstructure features of BCTWN ceramics (Figure 3a,b,c,d; Figure S15, Supporting information), respectively. The grain boundaries and *ab-plane* of grains could be roughly distinguished in PFM images, contributing to the structural analysis of domain structures in BCTWN ceramics. Based on the different out-of-plane and in-plane amplitude intensities and phase contrasts, the domain structures in the samples are clearly observed on the cross-sections of grains, which are highly consistent with the findings in Figure S13 (Supporting information). Specifically, in addition to the larger-size domain stripes with (110)-type DWs, the low-density (001)-type DWs are present in the BCTWN-0.00 ceramics with a lower d_{33}, while the BCTWN-1.75 ceramics with a super-high d_{33} exhibit high-density (001)-type DWs, leading to the presence of multi-domain states with small domain size and high DW density. It is worth noting that the (110)-type DWs on the cross-sections of grains, to some extent, are curved, possibly from the defect effects in ceramics, the same as the case in BIT single crystal reported elsewhere[36]. In order to observe the more detailed features, such intriguing domain architecture was characterized by bright-field (BF) TEM (Figure S16, Supporting information), clearly showing the distributions of (110)-type DWs and (001)-type DWs at nano-scale and further confirming the specific multi-domain states in BCTWN ceramics with high performance. Most importantly, the DWs possess a width of tens of nanometers and present a faceted shape with δ fringes, which is different from the DW features in classical PZT or BT ferroelectrics. Similar results have also been reported in pure BIT ferroelectrics[37].

Here, we believe the formation of such intriguing domain structures is closely connected with the super-high piezoelectric performance in BCTWN-1.75 ceramics. According to the classical ferroelectric domain theory ($D \propto \sqrt{E_{\mathrm{DW}}}$, where D denotes the domain size and E_{DW} represents the DW energy), the domain size is in direct proportion to the square root of DW energy in ferroelectrics, i.e., smaller domains possess lower DW energy with improved

polarization flexibility, thus beneficial to piezoelectric performance[38]. Combined with the theoretical point, we performed the local PFM lithography to reveal the ferroelectric domain switching behaviors in BCTWN ceramics (Figure S17, Supporting information). For the BCTWN ceramics with lower d_{33}, although a large proportion of ferroelectric domains are switched at the bias voltages of 30 or 40 V (Figure S17c,h, Supporting information), there remain several domains without reorientation at the higher bias voltages of 50 V (Figure S17h, Supporting information). For the BCTWN ceramics with super-high d_{33}, the ferroelectric domains are also partially switched at a smaller bias voltage of 30 V (Figure S17d,e,f, Supporting information), but the ferroelectric domain switching is totally saturated at a further increase of bias voltage such as 40 V (Figure S17f, Supporting information), suggesting its better polarization dynamic behaviors (such as easy polarization rotation and fast domain wall movement), which is undoubtedly inseparable from the presence of small-size multi-domain states with lower DW energy, thus leading to an excellent piezoelectric performance. Moreover, the flexible polarization dynamics also provide strong evidence for the lower coercive field of BCTWN-1.75 ceramics, as shown in Figure 2g. Therefore, we propose that the introduction of high-density layered (001)-type DWs and the formation of small-size multi-domain structures are mainly responsible for the super-high piezoelectric performance in BCTWN-1.75 ceramics.

To better understand the intriguing domain structures in BCTWN ceramics, we now attempted to unravel the underlying relationship between the DWs and two independent polarization vectors, $\mathbf{P}_a$ (a domain) and $\mathbf{P}_c$ (c domain) that simultaneously lie on the *ac plane* of the unit cell. Here, we performed BF- and dark-field (DF) TEM to probe ferroelectric domains under different zone-axes first and then elaborate structural features of the DWs. The domain stripes can be observed when the electron beam is aligned to the [001] zone-axis (Figure 3e; Figure S18a, Supporting information), while the DWs are not curved but almost straight, which lie on the (110) *plane* confirmed by the indication of corresponding selected area electron diffraction (SAED) pattern, clearly reflecting that only (110)-type DWs exist in this mode. Moreover, the interplanar spacing $d_{(200)}$ of 0.272 nm could be identified in the corresponding HRTEM image, revealing the atomic-scale structural features on the (001)

plane or *ab plane*. Note that the SAED pattern in Figure 3e is actually composed of the diffraction information in A-Region and B-Region, while the diffraction patterns of A-Region and B-Region can be rotated 90^o from the other one (Figure 3f), reflecting that the (110)-type DW belongs to the $\mathbf{P}_a$-90^o DW, which represents the 90^o rotation of a-domain at the DW. The possible polarization vectors $\mathbf{P}_a$ of the ferroelectric domains are indicated in the HRTEM image (Figure 3f), while no polarization vectors $\mathbf{P}_c$ lie on this crystallographic *plane*. Besides, in addition to the (110)-type 90^o DWs, the layered (001) DWs can be observed in the BF- and DF TEM image when the electron beam is aligned to the [010] zone-axis (Figure 3g; Figure S18c,d, Supporting information). Figure 3h shows the HRTEM image of a (001)-type DW across C-Region and D-Region in Figure 3g. Unlike the (110)-type DWs with 90^o rotation of a pair of twin-related ferroelectric variants, the diffraction patterns on both sides of the (001) DW keeps similar (Figure 3h), i.e., they can be approximately rotated 180^o from the other one, reflecting that the boundary between C-Region and D-Region is the $\mathbf{P}_a$-180^o DW, which represents the 180^o rotation of a-domain at the DW. According to the principle of the polarity that points to the (200) *disc* of convergent-beam electron diffraction (CBED) pattern in BIT[39], the polarization vectors $\mathbf{P}_a$ of such 180^o ferroelectric domains thus can be easily identified by the analysis of corresponding CBED patterns (Figure 3h). The possible polarization vectors $\mathbf{P}_a$ related to the (001) DW are thus indicated in Figure 3h. Besides, the polarization vectors $\mathbf{P}_c$ are commonly negligible due to their tiny piezoelectric contributions compared with the polarization vectors $\mathbf{P}_a$[40]. However, theoretically, they could exist on the crystallographic (010) *plane*, whose orientations are determined according to the structural analysis of corresponding FFT patterns (Figure 3h). Furthermore, the HRTEM image in Figure 3h with the periodic lattice fringes reveals the interplanar spacing $d_{(002)}$ of 1.641 nm, consistent with the atomic-scale observation in Figure 1b. Based on the above analysis, we accordingly propose the representative schematics of domain patterns in BCTWN ceramics with low and high piezoelectric performance, respectively (Figure 3i), contributing to a clear understanding of the structural origin of super-high piezoelectric performance and providing a general strategy to optimize electrical functionality by engineering domain structures, such as introducing high-density layered (001)-type 180^o DWs.

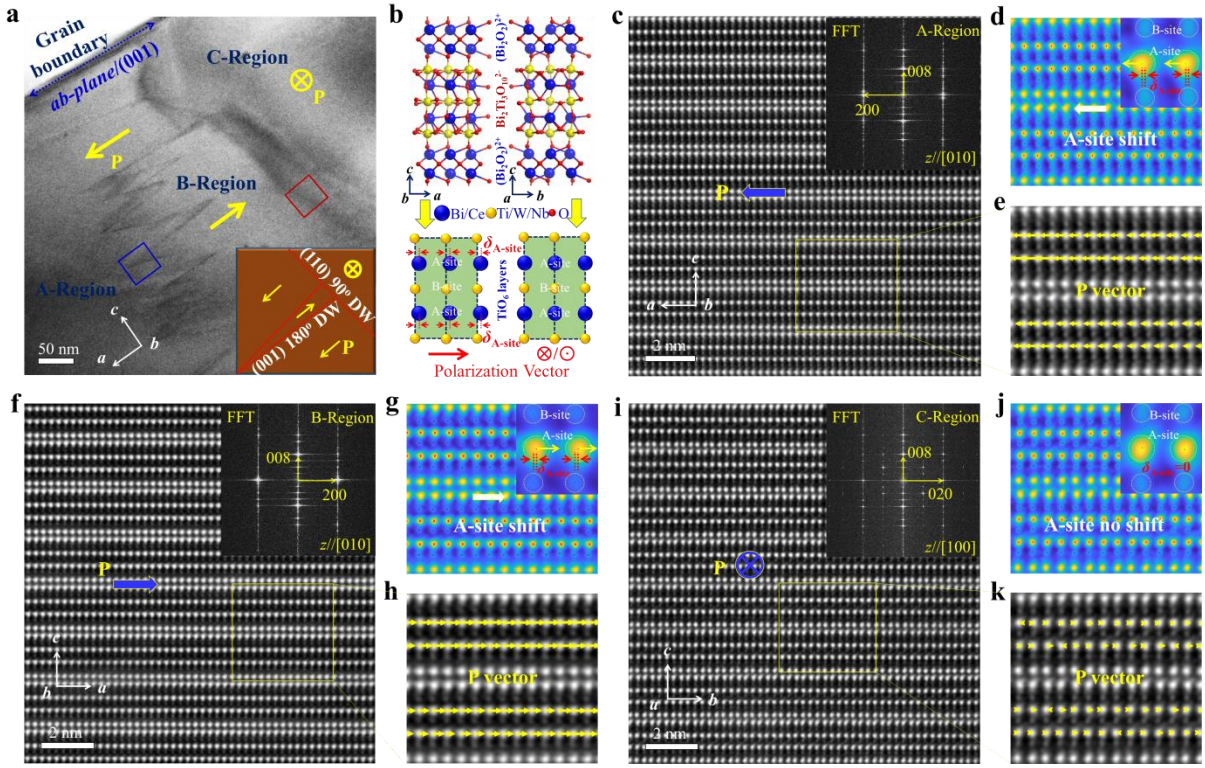

Figure 4. HAADF-STEM characterization of ferroelectric domains in BCTWN-1.75 ceramics. a) HAADF-STEM image of domain structures viewed along [010]/[100] zone-axis. The inset depicts the corresponding schematic of domain patterns. b) The schematics of crystal structure of BCTWN ceramics viewed along [010] and [100] zone-axes, respectively, with the displacement of A site ions ($\delta_{A\text{-site}}$) with respect to B site ions and corresponding polarization vector. c,f,i) Atomic-resolution HAADF-STEM images of A-, B-, and C-Region in (a), with the corresponding FFT patterns, respectively. d,g,j) 2D Gaussian peak fitting of atom columns of the yellow rectangular box in (c), (f), and (i), respectively. The insets represent the locally magnified peak fitting results, revealing the displacement directions of $\delta_{A\ site}$, respectively. e,h,k) Atomic-resolution polarization mapping of the yellow rectangular box in (c), (f), and (i), respectively.

Here, we also employed HAADF-STEM to directly observe the atom displacement inside each unit cell, which can convincingly uncover the local crystal ordering or polarization vectors inside ferroelectric domains at atomic-scale and further confirm the relationship between the DWs and polarization vectors. Figure 4a shows a low-magnification HAADF-STEM image taken along [010]/[100] zone-axis (Figure S19a,b, Supporting

information), revealing the intriguing domain structures with several wedge-shaped (001)-type DWs and a curved (110)-type DW, which are further disclosed by the locally magnified STEM images of blue- and red rectangular box in Figure 4a (Figure S19c,d, Supporting information). The observations are well consistent with the preceding analysis (Figure 3; Figure S13,14,15,16,18, Supporting information). For BIT ferroelectrics, due to the spontaneous polarization mainly stemming from the relative movement of three TiO_6 octahedral layers along *a* axis with respect to the Bi ions in perovskite layers[40], the displacement of A-site ions ($\delta_{A\text{-site}}$) with respect to B site ions in BCTWN ceramics can be thus used to express the polarization vector **P** in single unit cell, whose representative schematics are indicated in Figure 4b. Figure 4c shows an atomic-resolution HAADF-STEM image taken from the A-Region in Figure 4a, and the A/B-site atoms in perovskite layers are easily distinguished by the different image contrasts, as stated before (Figure 1c). To accurately locate the atom column positions in the sample, the intensity of each atom column can be fitted as a two-dimensional (2D) Gaussian peak[41]. The fitting results are shown in Figure 4d, with the calculated atom positions marked by the colored dots. The inset in Figure 4d shows the locally magnified $\delta_{A\text{-site}}$ and clearly reflects a leftward A-site ion shift, also indicating the orientation of polarization vector **P**. The atomic-resolution polarization mapping is thus determined, which is overlaid on the locally magnified HAADF-STEM image (Figure 1e), totally figuring out the ferroelectric domain with a leftward polarization vector in this region (Figure 1c). Likewise, for the atomic-resolution HAADF-STEM images taken from B- and C-Region in Figure 4a (Figure 4f,i), the corresponding atom column positions and polarization vector mapping can also be determined according to the 2D Gaussian peak fitting (Figure 4g,h,j,k), of which the A-site ions exhibit the rightward shifts in B-Region, reflecting the ferroelectric domain with a rightward polarization vector **P** in this region, while they present no evident shifts in C-Region, indicating the polarization vector **P** with out-of-plane orientation. It follows that the (001)-type DWs between A-Region and B-Region are constructed by a pair of 180^o twin-related ferroelectric domains, while the (110)-type DW between B-Region and C-Region is composed of a pair of 90^o twin-related ferroelectric domains. It means that the intriguing domain structures in BCTWN ceramics comprise (001)-type 180^o DWs and (110)-type 90^o DWs, which convincingly verifies the

structural analysis of TEM characterization in Figure 3e,f,g,h. The inset in Figure 4a shows a corresponding schematic of the domain structures with specific DW types, which also provides strong evidence for the domain patterns reconstructed in Figure 3i.

In addition to comprehensively elaborating the intriguing domain structures in BCTWN ceramics, we conclusively used the chemical etching technique to uncover the dynamic evolutions of the layered (001)-type 180^o DWs and (110)-type 90^o DWs at external fields. For the unpoled BCTWN ceramics, we have known that both (001)-type 180^o DWs and (110)-type 90^o DWs are observed on the cross-sections of grains (Figure S13b,20a, Supporting information), while the layered (001)-type 180^o DWs are almost disappeared after the ceramic is poled under external electric field (8 kV/mm), and only (110)-type 90^o DWs dominate the domain patterns in this case (Figure S20b,c, Supporting information). Interestingly, the (001)-type 180^o DWs emerge again after depoling treatment of BCTWN ceramics, once again located between the (110)-type 90^o DWs (Figure S20d, Supporting information). This dynamic evolution of domain structures directly suggests that the (001)-type 180^o DWs in BCTWN ceramics are easily switched and keep flexible polarization reaction under external stimulation, which is closely connected with their lower energy hierarchy compared with the (110)-type 90^o DWs, as the same case reported in BIT single crystal[42]. This further proves that the introduction of high-density (001)-type 180^o DWs substantially contributes to the enhanced piezoelectric performance of BCTWN ceramics. Besides, for ferroelectrics, the electrode interface generally is the main nucleation site of new ferroelectric domains during the polarization switching process at external electric fields[43]. However, fatigue behaviors tend to occur as the nucleation at the electrode interface is highly depressed after many polarization switching events at cyclic electric fields. For BCTWN-1.75 ceramics, the (110)-type 90^o DWs could provide additional nucleation sites of new ferroelectric domains in the fatigue switching process, since the (001)-type 180^o DWs with excellent polarization switching behaviors are easily nucleates at (110)-type 90^o DWs and grows between (110)-type 90^o DWs under external electric fields, which make the nucleation of new ferroelectric domains during electric fatigue cycles not solely dependent on the electrode interface, thereby leading to enhanced fatigue properties. Similar mechanisms have

also been revealed in La-doped BIT ferroelectrics[44], and we believe the introduction of high-density (001)-type 180^o DWs is also greatly responsible for the excellent fatigue resistance in BCTWN ceramics. In addition, it is widely known that decreasing the amount of oxygen vacancy by doping strategy is an effective strategy to enhance fatigue properties[45]. Therefore, for the BCTWN ceramics, in addition to the high density layered (001)-type DWs, the decrease in the concentration of oxygen vacancy due to the addition of high valence doping ions could be considered as another mechanism to enhance fatigue properties. The findings of (001)-type 180^o DWs on manipulating electrical performance are significantly innovative and perspective, and it is very expected for more novel designs of the (001)-type 180^o DWs *via* composition-driven domain engineering strategy further to optimize functionality properties in BIT-based ferroelectrics or other bismuth layered ferroelectrics in the near future.

3. Conclusion

In this work, we have successfully synthesized a series of $Bi_{3.96}Ce_{0.04}Ti_{3-0.02x}W_{0.01x}Nb_{0.01x}O_{12}$ (BCTWN) ceramics by the solid-state reaction technique. The layered crystal structure with a periodic arrangement of fluorite layers and perovskite layers along *c*-axis and atom column positions are revealed by HAADF- and ABF STEM as well as atomic-resolution EDS mapping. The lattice distortion depends on the dopant content, which is well-characterized by structural refinement and Raman spectra. The ceramic system possesses higher T_c (over 631 ^{o}C) and larger electrical resistivity (over 10^6 Ω·cm). Most importantly, it also attains super-high d_{33} of 38.5 pC/N (5 times larger than pure BIT ceramics), super-high d_{33}^* of 46.7 pm/V (at low electric field), and excellent fatigue stability (stable up to 10^7 cycles) at the optimal composition, which is a promising candidate for high-temperature applications that demand high-sensitivity and light-weight. Multi-scale microscopy characterization shows an intriguing domain configuration comprising striped (110)-type 90^o DWs and layered (001)-type 180^o DWs in BCTWN ceramics. It reveals that the introduction of high-density layered (001)-type 180^o DWs will significantly destroy long-range ordered (110)-type 90^o DWs, which induces the formation of small-size multi-domain states with low energy barriers, thereby contributing to the enhanced piezoelectric performance. In addition, the layered

(001)-type 180° DWs with flexible polarization rotation features are also responsible for the structural origin of superior fatigue stability. This work provides a general strategy for the future design of BIT ceramics with super-high performance *via* domain engineering.

4. Experimental Section

Sample Synthesis: $Bi_{3.96}Ce_{0.04}Ti_{3-0.02x}W_{0.01x}Nb_{0.01x}O_{12}$ (x=0.00, 0.50, 1.00, 1.50, 1.75, 2.00, 3.00, and 4.00; abbreviated as BCTWN-x) ceramics were prepared using the traditional solid-state method with appropriate amounts of Bi_2O_3 (99.999%), TiO_2 (99.99%), CeO_2 (99.999%), WO_3 (99%), Nb_2O_5 (99.99%) as the raw materials. The oxide powders were first mixed with ethanol by ball milling for 24 h, and then dried and calcined at 750~850 °C for 4 h. To get a homogenous compound, the mixtures were milled and dried again under the same conditions. After granulation using the polyvinyl alcohol (PVA, 8%), the powders were pressed into green pellets with a diameter of 10 mm and a thickness of 0.8 mm at 12 MPa. Finally, the green pellets were sintered at 1060~1140 °C for 4 h to get the BCTWN ceramics, wherein the sintering temperatures for BCTWN-x (x=0.00-4.00) are 1060 °C, 1100 °C, 1100 °C, 1120 °C, 1120 °C, 1100 °C, 1100 °C, and 1100 °C, respectively.

Electrical Properties: To characterize the electrical performance, the samples were coated with silver paste and then heated at 750 °C for 10 min to form surface electrodes. The dielectric properties were measured by an LCR analyzer (HP4980A, Agilent, USA) with frequencies of 10 kHz, 100 kHz, and 1MHz, at temperatures ranging from 25~700 °C. The dielectric temperature coefficient (Tk_ε) was expressed as[7e]

$$Tk_\varepsilon \frac{(\varepsilon_T - \varepsilon_{T_0})}{\varepsilon_{T_0}(T - T_0)}, \quad (1)$$

where ε_T and ε_{T_0} are the dielectric constants at applied temperature (T) and room temperature (T_0), respectively. The impendence behaviors were characterized by an LCR analyzer (HP4294A, Agilent, USA) at different temperatures, with further detailed analysis by Zview software. The DC resistivity (ρ) as a function of temperature was tested by an insulation resistance measurement system (HRMS-900, Partulab, China). The activity energy (E_a) was determined by the Arrhenius equation as follow[32]

$$\rho=\rho_0 \exp(\frac{E_a}{k_B T}), \quad (2)$$

where ρ_0 is the exponential factor and k_B denotes the Boltzmann constant. The piezoelectric coefficient (d_{33}) was measured by a quasi-static d_{33} meter (ZJ-3A, Institute of Acoustics, China) after the samples were poled under 6-8 kV/mm in silicone oil bath at 200 ^{o}C for 30 min. The polarization hysteresis (*P*-*E*) loops and strain-electric field (*S*-*E*) curves were carried out by a ferroelectric analyzer (TF2000, Aix ACCT, Aachen, Germany) with the frequency of 1 Hz, at 160 ^{o}C. The inverse piezoelectric coefficient (d_{33}^{*}) was defined as

$$d_{33}^{*}=\frac{S_{max}}{E_{max}}, \quad (3)$$

where S_{max} represents the maximum strain, and E_{max} is the maximum electric field. The electric fatigue experiment was also performed by the ferroelectric analyzer after electric cycles.

Structural Characterization: The natural surfaces of samples were characterized by scanning electron microscopy (SEM, JSM7500F, JEOL, Japan) at an acceleration voltage of 10 kV, and micro-scale energy-dispersive X-ray spectroscopy (EDS) elemental mapping was carried out by an EDS detector equipped on the SEM. The samples were polished to optical quality using polycrystalline diamond paste for the next characterization. First, the polished samples were treated by thermal etching at 950 ^{o}C for 3 h, and the surfaces of the samples were observed again by the SEM. After that, the polished samples were treated by chemical etching, of which HCl and HNO_3 are chosen as acid reagents with an etching time of around 3-5 minutes. The microstructure features, such as domain structures, were then detected by SEM and atomic force microscopy (AFM, NaioAFM, Nanosurf, Switzerland). In addition, the microstructures were also probed by optical microscopy (OM, Olympus-GX53, Japan). The phase structure was determined by X-ray diffraction (XRD, DX2700, Dandong, China) employing Cu*K*α radiation in the 2 theta range from 10~80^{o}. The XRD data was further refined by the Rietveld method utilizing commercial Maud software, with the CIF card #ICSD-159929. Raman spectra in the frequency range of 200~950 cm^{-1} were performed by a

Raman spectrometer (LabRAM HR, HORIBA, France) employing the 532 nm line from an Ar^+ laser as the excitation light source, and the resulting data was further analyzed by the Lorentz fitting.

Piezoresponse Force Microscopy (PFM) measurements: Before the PFM characterization, the samples were prepared using polished treatment. The PFM experiments were conducted *via* a commercial atomic force microscopy (AFM, MFP-3D, Asylum Research, USA) equipped with a PPP-EFM conductive probe (Nanosensors, Neuchatel, Switzerland) with a spring constant of 2.8 N/m and nominal resonance frequency of 70 kHz in air. The drive amplitude of 2.0 V and the scan rate of 1.0 Hz were set, with a transverse scan direction. Considering the polarization anisotropy of BIT ferroelectrics, both vertical PFM (VPFM) and lateral PFM (LPFM) images were attained by the dual AC resonance tracking (DART-PFM) mode. In addition, local PFM lithography was carried out to test domain switching behaviors. Two PFM litho patterns are used. One is a series of local bias voltages in a gradient of 15 V employed at virgin domains, where the maximum value is 30 V. However, the domain switching was not saturated. Therefore, in the second litho pattern, the maximum bias voltages were increased to 50 V. After the PFM litho process, the PFM phase images were recorded as same as the preceding conditions.

Transmission Electron Microscopy (TEM) and Scan TEM (STEM) measurements: The TEM sample was prepared successively by cutting, polishing, dimpling, and ion milling process. For the ion milling, the sample was carried out by a precision ion beam thinning system (PIPS Gatan 691, Gatan Inc., USA), with a voltage of 3.6~8 kV and an incident angle of $3\sim8^{o}$ for 2 h. The microstructural features of the ceramic sample were examined by TEM (Tecnai G2 F30, FEI, USA) at an acceleration voltage of 300 kV. The bright-field (BF) and dark-field (DF) TEM images were performed to identify the structural information of ferroelectric domains, and the high-resolution TEM (HRTEM) images were carried out to analyze the domain structures and crystal structures at atomic-scale. The convergent-beam electron diffraction (CBED) was employed to reveal the polarization orientations of ferroelectric domains. For STEM experiments, the sample was prepared by using a focused ion beam system (FIB, Helios NanoLab 600i, FEI, USA). High-angle annular dark-field

(HAADF) and annular bright-field (ABF) STEM images as well as atomic-resolution EDS mapping were performed by using an advanced STEM system (Titan Themis Z, FEI, USA) at an acceleration voltage of 300 kV. The microscope was equipped with a Schottky electron emitter, an electron energy monochromator, and a 5th-order probe spherical aberration corrector. The STEM resolution ranges from less than 60 pm, and the probe convergence and HAADF collection angles were 25.1 mrad and 65-200 mrad, respectively. The STEM images were corrected for possible drift and scanning beam distortions using a drift-corrected frame integration (DCFI) technique and were further proceeded by a radial wiener method in Velox software. The crystal structure models under different zone-axes were simulated by VESTA software. The atomic column positions in the STEM images were determined by two-dimensional (2D) Gaussian fitting, and the experimental intensity (*Z*) of each atom column could be fitted by the following Gaussian function[46]

$$Z(x,y) = A\exp\left(-\frac{(x-x_0)^2}{2\sigma_x^2} - \frac{(y-y_0)^2}{2\sigma_y^2}\right), \quad (4)$$

where *A* is the peak intensity, x_0 and y_0 are the peak position, σ_x and σ_y are the *x* and *y* spreads around the peak position. The fitting was carried out using Matlab software as described elsewhere[41b]. For BIT ferroelectrics, the polarization component from *c*-axis is negligible, since ion displacement along the vertical direction is very tiny[40]. Here, only the polarization component from *a*-axis is considered, and the ion displacement along the horizontal direction is calculated to determine the local crystal ordering and polarization vector.

Supporting Information

Supporting Information is available from the Wiley Online Library or from the author.

Acknowledgements

This work was supported by the National Natural Science Foundation of China (Grant Number 12102068), JSPS KAKENHI (Grant Number JP22KF0290), and KIBAN C (Grant Number JP22K03828).

Conflict of Interest

The authors declare no conflict of interest.

Data Availability Statement

The data that support the findings of this study are available from the corresponding author upon reasonable request.

References

[1] a) H. Yan, H. Zhang, R. Ubic, M. J. Reece, J. Liu, Z. Shen, Z. Zhang, *Advanced Materials* **2005**, 17, 1261; b) S. Zhang, F. Yu, *Journal of the American Ceramic Society* **2011**, 94, 3153; c) H. Wei, H. Wang, Y. Xia, D. Cui, Y. Shi, M. Dong, C. Liu, T. Ding, J. Zhang, Y. Ma, *Journal of Materials Chemistry C* **2018**, 6, 12446.

[2] S. Trolier McKinstry, S. Zhang, A. J. Bell, X. Tan, *Annual review of materials research* **2018**, 48, 191.

[3] a) L. Bian, X. Qi, K. Li, Y. Yu, L. Liu, Y. Chang, W. Cao, S. Dong, *Advanced Functional Materials* **2020**, 30, 2001846; b) D. Wang, Z. Fan, G. Rao, G. Wang, Y. Liu, C. Yuan, T. Ma, D. Li, X. Tan, Z. Lu, *Nano Energy* **2020**, 76, 104944; c) J. Shi, J. Liu, S. Xie, K. Chen, H. Zheng, B. Wu, J. Zhu, Q. Wang, *Journal of Alloys and Compounds* **2023**, 942, 169092; d) J. Liu, J. Shi, S. Xie, B. Wu, J. Zhu, Q. Wang, *Materials Characterization* **2023**, 195, 112474.

[4] a) X. He, C. Chen, L. Wang, Y. Gong, R. Dun, F. Zhang, Y. Wu, H. Zeng, Y. Li, Z. Yi, *Materials Today* **2022**, 58, 48; b) B. Aurivillius, *Arki Kemi* **1949**, 1, 463; c) N. A. Benedek, J. M. Rondinelli, H. Djani, P. Ghosez, P. Lightfoot, *Dalton Transactions* **2015**, 44, 10543; d) B. Park, B. Kang, S. Bu, T. Noh, J. Lee, W. Jo, *Nature* **1999**, 401, 682.

[5] a) S. Cummins, L. Cross, *Journal of Applied Physics* **1968**, 39, 2268; b) T. Jardiel, A. Caballero, M. Villegas, *Journal of the Ceramic Society of Japan* **2008**, 116, 511.

[6] H. Chen, B. Shen, J. Xu, J. Zhai, *Journal of Alloys and Compounds* **2013**, 551, 92.

[7] a) X. He, C. Chen, M. A. Boda, F. Zhang, Y. Gong, H. Zeng, Z. Yi, *Advanced Engineering Materials* **2022**, 24, 2200058; b) P. Xiang, Y. Kinemuchi, K. Watari, *Journal of the European Ceramic Society* **2007**, 27, 663; c) D. Jiang, Z. Zhou, R. Liang, X. Dong, *Journal of the European Ceramic Society* **2021**, 41, 1244; d) Y. Tang, Z. Shen, Q. Du, X. Zhao, F. Wang, X. Qin, T. Wang, W. Shi, D. Sun, Z. Zhou, *Journal of the European Ceramic Society* **2018**, 38, 5348; e) Q. Xu, S. Xie, F. Wang, J. Liu, J. Shi, J. Xing, Q. Chen, J. Zhu, Q. Wang, *Journal of Alloys and Compounds* **2021**, 882, 160637.

[8] a) M. Villegas, T. Jardiel, G. Farıas, *Journal of the European Ceramic Society* **2004**, 24, 1025; b) Q. Tang, Y. Kan, Y. Li, G. Zhang, P. Wang, *Scripta Materialia* **2006**, 54, 2075; c) L. Zhang, R. Chu, S. Zhao, G. Li, Q. Yin, *Materials Science and Engineering: B* **2005**, 116, 99.

[9] J. Hou, R. Kumar, Y. Qu, D. Krsmanovic, *Scripta Materialia* **2009**, 61, 664.

[10] X. Xie, Z. Zhou, R. Liang, X. Dong, *Journal of Materiomics* **2021**, 7, 59.

[11] J. Hou, Y. Qu, R. Vaish, D. Krsmanovic, R. V. Kumar, *Journal of the American Ceramic Society* **2011**, 94, 2523.

[12] R. Nie, J. Yuan, Q. Chen, J. Xing, J. Zhu, W. Zhang, *Journal of the American Ceramic Society* **2019**, 102, 5432.

[13] a) C. Deng, L. Ye, C. He, G. Xu, Q. Zhai, H. Luo, Y. Liu, A. J. Bell, *Advanced Materials* **2021**, 33, 2103013; b) H. Palneedi, M. Peddigari, G. T. Hwang, D. Y. Jeong, J. Ryu, *Advanced Functional Materials* **2018**, 28, 1803665; c) H. Pan, J. Ma, J. Ma, Q. Zhang, X. Liu, B. Guan, L. Gu, X. Zhang, Y. Zhang, L. Li, *Nature communications* **2018**, 9, 1813; d) D. Li, D. Zhou, W. Liu, P. Wang, Y. Guo, X. Yao, H. Lin, *Chemical Engineering Journal* **2021**, 419, 129601.

[14] a) Y. Liu, Y. Chang, F. Li, B. Yang, Y. Sun, J. Wu, S. Zhang, R. Wang, W. Cao, *ACS applied materials & interfaces* **2017**, 9, 29863; b) T. Zheng, H. Wu, Y. Yuan, X. Lv, Q. Li, T. Men, C. Zhao, D. Xiao, J. Wu, K. Wang, *Energy & Environmental Science* **2017**, 10, 528; c) H. Tao, H. Wu, Y. Liu, Y. Zhang, J. Wu, F. Li, X. Lyu, C. Zhao, D. Xiao, J. Zhu, *Journal of the American Chemical Society* **2019**, 141, 13987; d) K. Wang, J. F. Li, *Advanced Functional Materials* **2010**, 20, 1924; e) J. Wu, Z. Hu, X. Gao, Z. Chu, G. Dong, Z. Wang, B. Peng, R. Peng, Z. Zhou, S. Dong, *Acta Materialia* **2020**, 188, 416; f) H. Miao, S. Dong, F. Li, Journal of Applied Physics **2016**, 119.

[15] X. Xie, Z. Zhou, B. Gao, Z. Zhou, R. Liang, X. Dong, *ACS applied materials & interfaces* **2022**, 14, 14321.

[16] F. Zhang, W. Shi, S. Guan, Y. Xu, H. Yang, H. Chen, J. Xing, H. Liu, Q. Chen, *Journal of Alloys and Compounds* **2022**, 907, 164492.

[17] X. Xie, T. Wang, Z. Zhou, G. Cheng, R. Liang, X. Dong, *Journal of the European Ceramic Society* **2019**, 39, 957.

[18] F. Zhang, Y. Xu, H. Yang, S. Guan, W. Shi, Y. Chen, C. Huang, J. Xing, H. Liu, Q. Chen, *Journal of the American Ceramic Society* **2022**, 105, 4161.

[19]X. Xie, Z. Zhou, R. Liang, X. Dong, *Advanced Electronic Materials* **2022**, 8, 2101266.

[20]A. Watcharapasorn, P. Siriprapa, S. Jiansirisomboon, *Journal of the European Ceramic Society* **2010**, 30, 87.

[21]S. Xie, J. Xu, Y. Chen, Z. Tan, R. Nie, Q. Wang, J. Zhu, *Ceramics International* **2018**, 44, 16758.

[22]B. W. Lee, E. J. Lee, *Journal of Electroceramics* **2006**, 17, 597.

[23]Q. Xu, S. Xie, L. Li, J. Xing, Q. Chen, J. Zhu, Q. Wang, *Journal of the European Ceramic Society* **2023**, 43, 916.

[24]a) H. Sha, S. Liang, L. Liu, Z. Cheng, J. Zhu, R. Yu, *Micron* **2020**, 137, 102919; b) S. Xie, J. Shi, Q. Xu, Q. Wang, J. Zhu, Y. Sato, Q. Chen, *Scripta Materialia* **2022**, 217, 114793; c) D. Zhang, Y. Zhu, L. Liu, X. Ying, C. Hsiung, R. Sougrat, K. Li, Y. Han, *Science* **2018**, 359, 675.

[25]a) S. Pennycook, L. Boatner, *Nature* **1988**, 336, 565; b) I. Lazić, E. G. Bosch, S. Lazar, *Ultramicroscopy* **2016**, 160, 265; c) E. Yücelen, I. Lazić, E. G. Bosch, *Scientific reports* **2018**, 8, 1.

[26]E. Okunishi, I. Ishikawa, H. Sawada, F. Hosokawa, M. Hori, Y. Kondo, *Microscopy and Microanalysis* **2009**, 15, 164.

[27]a) M. Kitta, N. Taguchi, H. Sudrajat, H. Onishi, *Applied Physics Letters* **2021**, 118; b) W. Yang, X. Q. Tran, T. Yamamoto, S. Yoshioka, F. Somidin, K. Nogita, S. Matsumura, *Physical Review Materials* **2020**, 4, 065002.

[28]H. Xue, L. Jiang, G. Lu, J. Wu, *Advanced Functional Materials* **2023**, 33, 2212110.

[29]K. Zhu, M. Zhang, Y. Deng, J. Zhou, *Physica B: Condensed Matter* **2010**, 405, 1388.

[30]M. Li, M. Pietrowski, R. De Souza, H. Zhang, I. Reaney, S. Cook, J. Kilner, D. Sinclair, *Nature materials* **2014**, 13, 31.

[31]X. Li, L. Zhu, P. Huang, Z. Chen, W. Bai, L. Li, F. Wen, P. Zheng, W. Wu, L. Zheng, *Journal of Applied Physics* **2020**, 127.

[32]H. Shulman, M. Testorf, D. Damjanovic, N. Setter, *Journal of the American Ceramic Society* **1996**, 79, 3124.

[33]a) Z. Shen, Z. Zhang, C. Qin, W. Luo, F. Song, Z. Wang, Y. Li, *Journal of Materials Research* **2021**, 36, 1134; b) Z. Peng, Y. Chen, Q. Chen, N. Li, X. Zhao, C. Kou, D. Xiao, J. Zhu, *Journal of Alloys and Compounds* **2014**, 590, 210; c) Z. Peng, Q. Chen, Y. Chen, D.

Xiao, J. Zhu, *Materials Research Bulletin* **2014**, 59, 125; d) S. Xie, J. Xu, Y. Chen, L. Jiang, Z. Tan, R. Nie, Q. Xu, Q. Wang, J. Zhu, *Ceramics International* **2018**, 44, 20432; e) Y. Zhao, H. Fan, G. Dong, Z. Liu, *Materials Letters* **2016**, 174, 242.

[34]C. Long, H. Fan, M. Li, G. Dong, Q. Li, *Scripta Materialia* **2014**, 75, 70.

[35]a) S. Xie, Y. Chen, W. Liu, G. Xia, B. Huang, C. Liu, Q. Wang, J. Li, *Acta Materialia* **2020**, 188, 228; b) S. Xie, Z. Tan, L. Jiang, R. Nie, Q. Xu, Y. Chen, J. Zhu, Q. Wang, *Ceramics International* **2020**, 46, 1183.

[36]S. Katayama, Y. Noguchi, M. Miyayama, *Advanced Materials* **2007**, 19, 2552.

[37]D. Su, Y. Ding, J. Zhu, Y. Yao, P. Bao, J. Liu, Y. Wang, *Journal of Physics: Condensed Matter* **2004**, 16, 4549.

[38]W. Cao, C. A. Randall, *Journal of Physics and Chemistry of Solids* **1996**, 57, 1499.

[39]W. Ye, C. Lu, Y. Zhang, Y. Zhou, *Journal of Applied Crystallography* **2015**, 48, 1080.

[40]Y. Noguchi, T. Goto, M. Miyayama, A. Hoshikawa, T. Kamiyama, *Journal of Electroceramics* **2008**, 21, 49.

[41]a) C. Jia, S. Mi, K. Urban, I. Vrejoiu, M. Alexe, D. Hesse, *Nature materials* **2008**, 7, 57; b) S. Zhang, Y. Zhu, Y. Tang, Y. Liu, S. Li, M. Han, J. Ma, B. Wu, Z. Chen, S. Saremi, *Advanced Materials* **2017**, 29, 1703543.

[42]W. Ye, L. Tang, C. Lu, H. Li, Y. Zhou, *Journal of Applied Crystallography* **2016**, 49, 1645.

[43]E. Colla, D. Taylor, A. Tagantsev, N. Setter, *Applied Physics Letters* **1998**, 72, 2478.

[44]Y. Ding, J. Liu, H. Qin, J. Zhu, Y. Wang, *Applied Physics Letters* **2001**, 78, 4175.

[45]T. Sreesattabud, B. Gibbons, A. Watcharapasorn, S. Jiansirisomboon, *Ceramics International* **2013**, 39, S521.

[46]S. M. Anthony, S. Granick, *Langmuir* **2009**, 25, 8152.